Original papers

Granular Matter 6, 1–9 © Springer-Verlag 2004
DOI 10.1007/s10035-003-0151-9

The liquefaction cycle and the role of drainage in liquefaction

Roel Snieder, Annemieke van den Beukel

Abstract In this work the liquefaction cycle is introduced as a framework to describe the coupled processes that take place in fluid-saturated granular media that lead to liquefaction. The modular formulation of liquefaction makes it possible to test the various processes that contribute to liquefaction separately, and to assemble different formulations of the relevant physics into a numerical model for liquefaction. This view on liquefaction is used here to assess the role of drainage in liquefaction. We present a simple scale analysis of the role of drainage. A numerical implementation of the liquefaction cycle shows, however, that the scale analysis is deceptive for the case when strong spatial variations in the permeability inhibit fluid migration. As an illustration the numerical model is used to quantify the imprint of a low-permeability layer on the liquefaction behavior.

Keywords Liquefaction, Phase transitions, Earthquake hazard

1 Introduction

Liquefaction is a phase transition in a water-saturated, loosely packed granular soil that turns the initially solid soil into a liquid. In this coupled process, the buildup of excess pore pressure by the compaction of the soil causes the shear modulus to decrease dramatically. If an earthquake strikes an area that is susceptible to liquefaction, extensive damage to structures and buildings may occur [1–3]. Testing procedures have been developed to estimate the susceptibility of a certain soil to liquefaction [4,5]. A key issue in the onset and consequences of liquefaction is played by drainage. Fluid migration suppresses variations in the excess pore pressure. Therefore, drainage may delay or prevent the onset of liquefaction. Laboratory experiments to assess the liquefaction potential of soil under undrained conditions [6] may give a biased assessment of the liquefaction potential of the soil. For this reason, the role of drainage on liquefaction is investigated in this paper.

To reach the goal of better understanding the process of liquefaction, roughly two types of studies have been carried out in the past: experiments on soil samples and modeling of field situations where liquefaction is known to have occurred. An overview of laboratory test procedures is given by Das [7]. A shortcoming of many of these experiments is that they deal with the relation between two factors that influence liquefaction, e.g. number of cycles of load application and excess pore pressure buildup, without linking these aspects into a physical description of liquefaction. Although this approach can be useful from a pragmatic point of view, it is not clear to what extent such measurements can be generalised to the in situ conditions in the subsurface. The other type of study, field measurements (e.g. [8,9]), concentrate on a particular soil and event with the aim to explain how and why liquefaction has occurred. Such studies often employ empirical relations between in situ soil engineering tests and the susceptibility to liquefaction. In some cases these relations work well and are able to predict the occurrence of liquefaction given a certain event and soil. The implementation of parameterized empirical relations has led to numerical models that simulate liquefaction with great accuracy (e.g. [10]). However, the complexity of these models makes it difficult to gain physical insight into the process of liquefaction.

In this work the concept of the liquefaction cycle is introduced as a theoretical framework for liquefaction in which the different processes that contribute to liquefaction can clearly be identified and are amendable to laboratory studies or a theoretical analysis. The liquefaction cycle translates into a system of coupled partial differential equations that can be solved numerically. An implementation is presented for a stratified earth model with a vertically incident SH-wave [11]. In that case all quantities depend on one space dimension only. This simple model gives insight into the role of drainage in liquefaction. The formulation employed here can easily be generalised to situations where lateral variations are relevant.

Recieved: 15 March 2003

R. Snieder (✉), A. van den Beukel
Department of Geophysics and Center for Wave Phenomena,
Colorado School of Mines,Golden, CO 80401, USA
e-mail: rsnieder@mines.edu
Tel.: +1-303-273.3456
Fax: +1-303-273.3478

We greatly appreciate our conversations with Masami Nakagawa and Vaughan Griffiths about this work. The critical and constructive comments of two anonymous reviewers are very much appreciated. The visit of Annemieke van den Beukel to Golden was supported by the Molengraaff fonds, the Schuurman Schimmel van Outeren Stichting, the Stichting Dr. Hendrik Muller's Vaderlandsch Fonds, and the Trajectum Fonds.

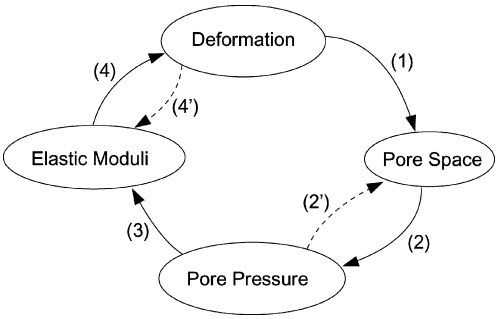

Fig. 1. The chain of events that form the liquefaction cycle. The links indicated with solid lines have been taken into account in this study, while the links indicated with dashed lines have been ignored

One advantage of the modular approach taken here is that it may help in obtaining a better understanding which of the coupled processes that contribute to liquefaction is understood well, and which processes require more research.

2 The liquefaction cycle

The liquefaction cycle as shown in Fig. 1 is based on a reductionists formulation [12] where the complex process of liquefaction is broken down into sub-processes that are easier to understand and to verify experimentally. The process of liquefaction can be described by the following chain of events. The deformation of the soil leads to a change in the pore space. During liquefaction the pore space generally decreases. This process is indicated by link 1 in the liquefaction cycle. A reduction of the pore space leads to an increased pore pressure (link 2). If the fluid cannot migrate, the increase in the pore pressure follows from the compression of the pore fluid due to reduction of the pore volume as described by the bulk modulus. However, the fluid migration associated with drainage in general reduces the maxima in the pore pressure. An increased pore pressure reduces the shear stress the grains can support, and leads in the elastic regime to a reduction of the shear modulus (link 3). A change in the elastic moduli, in its turn, leads to a modification of the deformation of the soil (link 4). The links (1–4) from a continuous positive feedback loop.

The links (1–4) suggest a circular chain of cause-effect relations. In reality the situation may be more complex and other feedback loops may play a role. An example is shown as link 2' in the liquefaction cycle that describes the effect of pore pressure on compaction, and link 4' that accounts for the shear weakening or shear hardening that is caused by the deformation. In the following subsections the different links in the liquefaction cycle are described in more detail.

2.1 Link 1, compaction

The compaction associated with liquefaction is induced dynamically, it should not be confused with the compaction of soils due to a static loading [13]. The compaction under a static load is governed to a large extent by the pore pressure [14–16]. In contrast to this, the compaction during liquefaction is induced by dynamic shear [3]. Although the resulting compaction will be influenced by the pore pressure as well (link 2' in the liquefaction cycle), we ignore this effect in this study. The compaction of soil due to the combined influence of shear and pore pressure is arguably the link in the liquefaction cycle that is most poorly understood.

The compaction of soil due to shear has been modelled on a microscopic scale using the Distinct Element Method [17]. Here we use the macroscopic formulation of compaction of Knight et al. [18] who measured the compaction of column of glass beads that was subjected to vertical tapping. They found that the grain fraction φ was described well by the following compaction law

$$\varphi(t) = \varphi_f - \frac{\varphi_f - \varphi_0}{1 + B \ln\left(1 + \frac{t}{\tau}\right)} , \qquad (1)$$

where φ_0 and φ_f are the initial and final grain fraction, respectively, B and τ are material-dependent parameters, and t denotes the duration of the deformation. This is equivalent to the number of taps delivered to the column. The grain fraction is defined as the volume of the grains divided by the total volume, hence $\varphi = 1/(1+e)$, with e the void ratio (defined as the ratio of the volume of the pores divided by the volume of the grains). Liquefaction is mostly influenced by shear motion rather than longitudinal motion [19]. Nicolas et al. [20] studied the compaction of a system of glass beads that was subjected to a periodic shear motion. They showed that the resulting compaction was described well by the compaction law (1). Several theories based on different arguments account for this compaction law [21–26].

Up to this point, compaction data have been used that were based on experiments with glass beads. In order to make the connection with the compaction of a soil we use the compaction measurements of Youd [27] who subjected sand to a periodic shear motion with a variable strain. The resulting grain fraction for a loading of 1, 30 and 1000 cycles is shown in Fig. 2 as a function of the maximum strain per cycle.

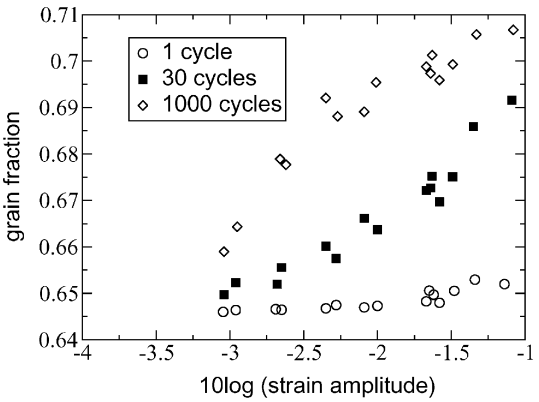

Fig. 2. The grain fraction of sand as measured by Youd (1972) for 1, 30 and 1000 shear cycles as a function of the maximum strain per cycle

The compaction law (1) is unsatisfactory in the sense that it gives the compaction as a function of time, or equivalently, the number of deformation cycles, but it does not account explicitly for the strength of the deformation in each cycle. We make the assumption that the compaction depends on the accumulated deviatoric strain. This quantity is given by $\int_0^t |\partial\varepsilon/\partial t'|\, dt'$, where ε denotes the deviatoric strain. For this reason we generalise the compaction law (1) in the following way to include the effect of a varying shear strength

$$\varphi(t) = \varphi_f - \frac{\varphi_f - \varphi_0}{1 + B\ln(1 + C\int_0^t |\partial\varepsilon/\partial t'|\, dt')} \,. \tag{2}$$

For a sinusoidally varying strain with period T and maximum $\varepsilon_{\max}$ one finds by direct integration that $n\varepsilon_{\max} = \int_0^t |\partial\varepsilon/\partial t'|\, dt'/4$, where the number of shear cycles is given by $n = t/T$. With these expressions the data of Youd [27] can be related to the compaction law (2). A least-squares fit of the data shown in Fig. 2 to the compaction law depicted in Fig. 3 shows that the compaction of sand is well-described by the compaction law (2). This fit is based on the following parameters: $\varphi_f = 0.8$, $\varphi_0 = 0.646$, $B = 0.09$, and $C = 12.5$.

Note that this compaction law connects the measurements for 1 cycle and 30 cycles well. The compaction for 30 cycles and 1000 cycles is not connected equally well. Since the strong ground motion due to earthquakes lasts usually for at most a hundred cycles [28], we employ the compaction law (2) in this study. In this law the grain fraction increases monotonically with the accumulated shear. However, for large deformation granular media may expand due to grain sliding. This may result in 'dilative arrest' of liquefaction [3]. In order to incorporate this phenomenon a more complex compaction law needs to be used.

2.2
Link 2, buildup of excess pore pressure

Rather than using an experimental law for the excess pore pressure [29] we derive the development of excess pore pressure from first principles. In the absence of drainage, the change in the pore pressure is given by the relative change in the volume of the pore fluid:

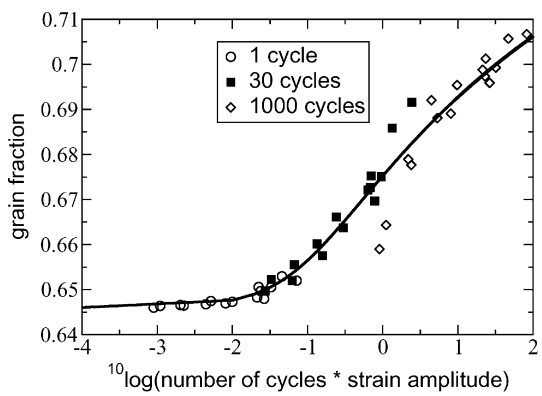

Fig. 3. The grain fraction of sand as measured by Youd (1972) for 1, 30 and 1000 shear cycles as a function of the maximum stain per cycle times the number of cycles. The compaction described by expression (2) is shown by a solid line

$$\dot{p} = -\kappa\frac{\dot{V}}{V} \,, \tag{3}$$

where κ is the bulk modulus of the fluid and V the volume of the pore fluid. When the pore fluid contains air, the bulk modulus of the fluid-air mixture needs to be used. When the fluid migrates, the change in the volume of the pore fluid is affected by the change in the available pore space as well as by the fluid migration. This means that the rate of change in the pore fluid volume is given by

$$\frac{\dot{V}}{V} = -\dot{\varphi} + \nabla\cdot\mathbf{v}_f \,. \tag{4}$$

In this expression, φ is the grain fraction introduced in section 2.1 and $\mathbf{v}_f$ is the velocity of the fluid flow. Using Darcy's law [30], the fluid flow can be expressed in the pressure gradient

$$\mathbf{v}_f = -\frac{K}{g\rho_f}\nabla p \,, \tag{5}$$

with K the hydraulic conductivity of the soil and ρ_f the mass density of the pore fluid. Combining the expressions (3)–(5) gives a diffusion equation for the pressure

$$\frac{\partial p}{\partial t} = \kappa\left(\nabla\cdot\frac{K}{g\rho_f}\nabla p\right) + \kappa\frac{\partial\varphi}{\partial t} \,. \tag{6}$$

The equation is equivalent to expression (4.65) of Wang [16]. Note that the rate of change of compaction $\partial\varphi/\partial t$ acts as a source term in this expression.

In the subsurface, the hydraulic conductivity K can vary with several orders of magnitude over short distances [30]. It should be noted that the permeability is present within the divergence in expression (6) and that taking the permeability outside the divergence [31] can lead to significant errors.

2.3
Link 3, changing the elastic moduli

Following Terzaghi's effective stress principle [32], the increase of excess pore pressure diminishes the effective stress σ', which reduces the shear modulus μ. In general, for saturated granular soils, the change of shear modulus with effective stress follows a power-law relation [33, 34], with exponent between 0 and 1. The exponent for a pure and dry sand, measured in the laboratory [7,19], is approximately 0.5:

$$\mu = A\sigma'^{0.5} \,, \tag{7}$$

where A is a constant and the effective stress is given by

$$\sigma' = \rho_d g z - p \,. \tag{8}$$

In this expression ρ_d is the mass density of the dry matrix and p is the excess pore pressure. The square root relation (7) falls in the range of measurements for saturated sand. The model soil will initially, in the absence of excess pore pressure ($p = 0$), have a shear modulus profile that increases with the square root of depth

$$\mu_0(z) = A\sqrt{\rho_d g z} \,. \tag{9}$$

When the excess pore pressure builds up, the shear modulus decreases depending on the excess pore pressure, and the shear modulus is given by

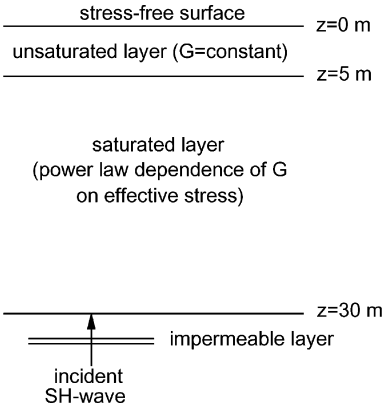

Fig. 4. The geometry of the model used in the numerical simulation

$$\mu = \mu_0(z)\left(1 - \frac{p}{\rho_d g z}\right)^{0.5} . \tag{10}$$

The value of the exponent depends strongly on the characteristics of the soil [34] and that a different value of the exponent may be appropriate for a particular soil.

The consequence of a power-law relation (9) is a shear modulus that vanishes at the surface. This poses problems in numerical modelling the liquefaction cycle. We circumvent these problems by assuming that the near-surface layer is unsaturated (Fig. 4) and has a shear modulus that is independent of depth and does not vary with time.

2.4 Link 4, deformation of the soil

The deformation of the soil follows from Newton's law

$$\rho\ddot{\mathbf{u}} = \nabla \cdot \tau , \tag{11}$$

where $\mathbf{u}$ denotes the displacement and τ the stress tensor. When the medium behaves elastically, the stress follows by Hooke's law

$$\tau_{ij} = c_{ijkl}\partial_k u_l + \tilde{c}_{ijkl}\partial_k v_l , \tag{12}$$

with c_{ijkl} the elasticity tensor. The last term is proportional to the particle velocity $\mathbf{v}$, this term is introduced to include viscous dissipation. This term effectively leads to complex elastic moduli that account for hysteresis of the soil. The numerical implementation of section 4 is based on equations for the first time derivative of the velocity and the stress, respectively. Newton's law (11) is written in component form as

$$\rho\dot{v}_i = \partial_j \tau_{ji} . \tag{13}$$

If the elastic medium is isotropic, and if the viscous dissipation depends on the shear stress only, the time-derivative of (12) is given by

$$\dot{\tau}_{ij} = \lambda\delta_{ij}(\nabla \cdot \mathbf{v}) + \mu(\partial_i v_j + \partial_j v_i) + \nu(\partial_i \dot{v}_j + \partial_j \dot{v}_i) , \tag{14}$$

where ν denotes the viscosity.

For a given angular frequency ω, the viscosity can be related to the quality factor Q by considering a plane shear wave that propagates through a homogeneous medium: $\mathbf{v} = \hat{\mathbf{y}} \exp i(kz - \omega t)$ into the equations (13) and (14). This solution has a complex wave number k and decays with a damping term $\exp(-\nu\omega z/2\mu c)$, with $c = \sqrt{\mu/\rho}$ the shear velocity. This implies that the quality factor is related to the viscosity by

$$Q = \frac{\mu}{\omega\nu} . \tag{15}$$

Note that the link described in this section describes elastic behaviour (with a simple anelastic damping), whereas the compaction treated in section 2.1 is a complex aneleastic phenomenon. Both processes take place at a different time scale, the period of the waves and the time scale of the compaction, respectively. The physics underlying these processes is of a different nature. After the onset of liquefaction, the elastic treatment of this section is no more applicable and plasticity phenomena need to be incorporated into the theory.

3 Scale analysis for drainage

Before embarking on the numerical implementation of the liquefaction cycle, it is interesting to consider the role of drainage with a simple scaling argument. The evolution of the excess pore pressure is governed by equation (6). The first term on the right hand side accounts for the change in the pressure due to the fluid flow, while the last term account for the influence of the compaction. A dimensionless measure of the relative importance of the drainage is thus given by the ratio

$$F = \kappa \frac{\left(\nabla \cdot \frac{K}{g\rho_f}\nabla p\right)}{\partial p/\partial t} . \tag{16}$$

When $F > 1$ drainage is important.

Let the thickness of the liquefying layer be denoted by L, the time scale of the liquefaction process by T, then the ratio (16) is of the order

$$F \sim \frac{\kappa K T}{g\rho_f L^2} . \tag{17}$$

Using the bulk modulus of water ($\kappa = 2.25 \times 10^9 kg/ms^2$) and assuming the values $T = 5\ s$ and $L = 5\ m$, it follows that $F \sim K \times 4.5 \times 10^4\ s/m$. Drainage is significant when this ratio is larger than unity, this happens when the hydraulic conductivity is given by.

$$K > 2 \times 10^{-5} m/s \tag{18}$$

For clean sands the hydraulic conductivity varies from $10^{-5} - 10^{-2}\ m/s$ [30]. This means that the range of hydraulic condictivity for clean sands is such that drainage may be important, depending on the spatial and temporal scales of the liquefaction zone. This implies that it is not obvious that laboratory tests under undrained conditions on desktop-size samples give a reasonable impression of the onset of liquefaction in field conditions where drainage can play an important role. For this reason more detailed numerical models are needed to assess the role of drainage in liquefaction. A small amount of trapped air may lower the bulk modulus κ. Acording to expression (17) this reduces the importance of drainage in liquefaction.

4
A numerical model of liquefaction

The numerical modelling presented here is for the simplest case of a soil whose properties depend on depth only, for the special case of a vertically incident SH-wave that is polarized in the y-direction [11]. The relevant dynamical parameters for the wave propagation are the particle velocity v in the y-direction and the stress component τ_{yz} which for brevity is denoted by τ. For this special case all quantities depend on the space variable z only. For example, the only nonzero strain components are $\varepsilon_{yz} = \varepsilon_{zy} = 1/2\partial v/\partial z$. This gives $|\dot{\varepsilon}| = \sqrt{\varepsilon_{yz}^2 + \varepsilon_{zy}^2} = |\partial v/\partial z|/\sqrt{2}$. The equations (2), (6), (10), (13), and (14) are for this special case given by

$$
\begin{aligned}
\varphi(t) &= \varphi_f - \frac{\varphi_f - \varphi_0}{1 + B\ln(1 + C\int_0^t |\partial v/\partial z|\, dt'/\sqrt{2})} \\
\frac{\partial p}{\partial t} &= \kappa\left(\nabla\cdot\frac{K}{g\rho_f}\nabla p\right) + \kappa\frac{\partial\varphi}{\partial t} \\
\mu &= \mu_0(z)\left(1 - \frac{p}{\rho_d g z}\right)^{0.5} \\
\frac{\partial v}{\partial t} &= \frac{1}{\rho}\frac{\partial\tau}{\partial z} \\
\frac{\partial\tau}{\partial t} &= \mu\frac{\partial v}{\partial z} + \nu\frac{\partial}{\partial z}\left(\frac{1}{\rho}\frac{\partial\tau}{\partial z}\right)
\end{aligned}
\tag{19}
$$

In the last expression the time derivative $\dot{v}$ has been eliminated with Newton's law (13). Note that the last expression is a forced diffusion equation similar to the expression in the second line for the excess pore pressure.

The computational domain runs from the surface $z = 0$ to a depth $z = H$, see Fig. 4. The equations (19) need to be supplemented with boundary conditions at these two depths. At the free surface, both the excess pore pressure p and the stress τ vanish. We assume that the saturated soil overlays an impermeable layer at the bottom. In that situation there is no flow at the bottom and $\partial p/\partial z = 0$ at that location. The last boundary condition that needs to be supplied is for the particle velocity at the bottom of the domain. We assume that the velocity at that location is given by the sum of an upward moving incoming wave v_{inc}, plus waves that are radiated downward: $v = v_{inc}(z + ct) + v_{down}(z - ct)$ and $\tau = \tau_{inc}(z + ct) + \tau_{down}(z - ct)$. The incoming wave v_{inc} acts as the source of the motion in the soil. The last term provides a radiation boundary condition [35] for the reflected waves. Using (19) the down going wave satisfies $\partial v_{down}(z - ct)/\partial t = \rho^{-1}\partial\tau_{down}(z - ct)/\partial z = -(\rho c)^{-1}\partial\tau_{down}(z - ct)/\partial t$. Integrating this identity shows that at the bottom of the domain $v_{down} = -(\rho c)^{-1}\tau_{down}$. With a similar argument one finds that $v_{inc} = +(\rho c)^{-1}\tau_{inc}$. Therefore at the bottom of the domain $v = v_{inc} + v_{down} = v_{inc} - (\rho c)^{-1}\tau_{down} = v_{inc} - (\rho c)^{-1}(\tau - \tau_{inc}) = 2v_{inc} - (\rho c)^{-1}\tau$. Using these results the boundary conditions are given by

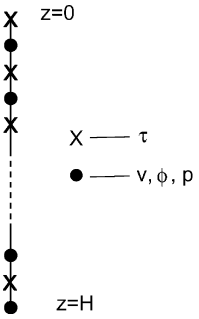

Fig. 5. The staggered grid used in the numerical modelling. The various physical properties are evaluated at the indicated grid points

$$
\begin{aligned}
&p(z = 0) = 0\,, \\
&\tau(z = 0) = 0\,, \\
&\frac{\partial p}{\partial z}(z = H) = 0\,, \\
&v(z = H) = 2v_{inc}(z = H) - \frac{1}{\rho c}\tau(z = H)\,.
\end{aligned}
\tag{20}
$$

The equations (19) with the boundary conditions (20) are solved on the staggered grid shown in Fig. 5 using the numerical scheme of Virieux [36] where the time-stepping is carried out with a leapfrog scheme [37]. In all simulations the model depth was $H = 30\ m$, the time step was $\Delta t = 5 \times 10^{-4}\ s$, the depth discretization $\Delta z = 1m$, and the density of the dry matrix was $\rho_d = 2000\ kg/m^3$. In all simulations the water table was taken at a depth of $z = 5\ m$, the shear modulus in the unsaturated layer above that depth was set to a constant value independent of depth and time. The viscosity ν was related to the quality factor (15) where Q was, modified after Das [7], taken to be

$$
Q = \frac{Q_0}{\left[1 - C(\rho g z - p)\,|\varepsilon|^{0.3}\right]}\,, \tag{21}
$$

with the following values for the parameters: $Q_0 = 1.8567$, and $C = 1.6937 \times 10^{-6}\ Pa^{-1}$.

5
Simulation for constant permeability

The first numerical simulation shown in this section is for a constant hydraulic conductivity of $K = 5 \times 10^{-4}\ m/s$. The incoming wave v_{inc} is shown in Fig. 6 as a function of time. This waveform is generated synthetically by bandpass filtering Gaussian white noise between frequencies of $1\ Hz$ and $20\ Hz$. The amplitude is normalised in such a way that the peak ground acceleration is about $0.1g$, a realistic value for earthquake hazard studies. The resulting waveform qualitatively resembles the strong motion generated by earthquakes [28].

The grain fraction φ as a function of depth at $t = 5.33\ s$ is shown in Fig. 7. Note that the compaction varies with depth, and that the relative change in the grain fraction due to the compaction is of the order 10^{-3}, so that the soil does not compact much. However, the associated excess pore pressure shown in Fig. 8 is comparable to the overburden pressure for the dry matrix at a depth of about $12\ m$. The reason for the large increase in pressure for a

modest amount of compaction is the large numerical value of the bulk modulus κ. A modest amount of air trapped in the fluid would significantly reduce the value of the bulk modulus.

At a depth of about 12 m, the excess pore pressure is comparable to the overburden pressure. This means that about this depth the soil will liquefy. This can be seen in Fig. 9 which shows the shear modulus before the shaking, and at $t = 5.33$ s. At a depth around 12 m the shear modulus has decreased dramatically and the shear strength of the soil is strongly diminished at the depth. The temporal behavior of the excess pore pressure at a depth of 12 m is shown in Fig. 10. It can be seen that the excess pore pressure approaches the overburden pressure at $t = 5.33\,s$.

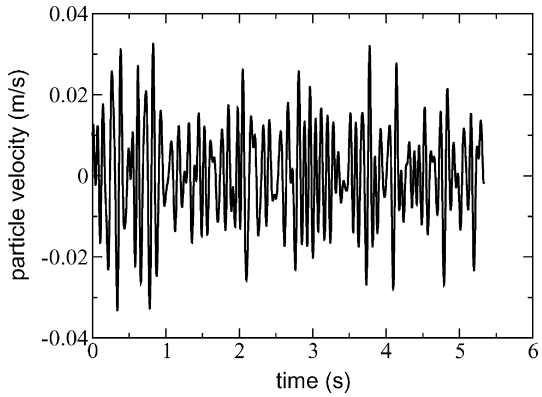

Fig. 6. The incident SH-wave v_{inc} used in the numerical examples that strikes the bottom of the domain

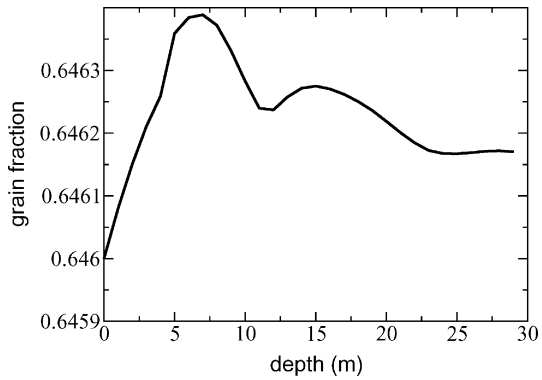

Fig. 7. The grain fraction at $t = 5.33$ s as a function of depth

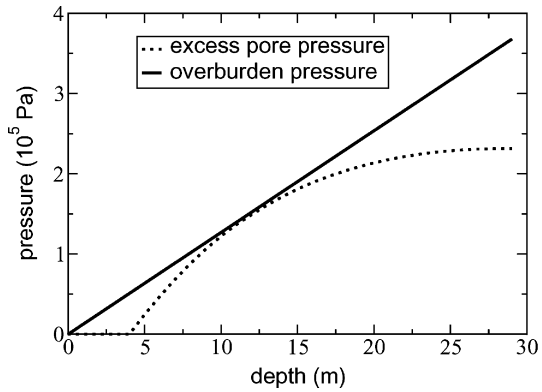

Fig. 8. The excess pore pressure at $t = 5.33$ s as a function of depth

The time scale to be used for a scale analysis in section 3 is given by the time over which the excess pore pressure steadily increases, in this case about 5 s. Note that the excess pore pressure does not increase monotonically. The compaction law (2) prescribes a grain fraction that increases monotonically with time. In the absence of flow this would imply a monotonic increase of the excess pore pressure with time. The fluctuations of the excess pore pressure with time that lead to short-term reductions of the excess pore pressure are therefore cause by fluid migration.

The scale analysis of section 3 shows that a hydraulic conductivity of the order of 2×10^{-5} m/s separates the regime where drainage inhibits liquefaction from the regime where liquefaction will occur. This scale analysis is relatively crude. Here we investigate this issue in more detail by showing numerical simulation for the incoming wave of Fig. 6 for a hydraulic condictivity given by $K = 10^{-5}, 10^{-4}, 10^{-3}$ m/s. These values are realistic for clean sand [30]. The excess pore pressure as a function of time at a depth of 8 m is shown in Fig. 11. For a hydraulic conductivity of 10^{-5} m/s the excess pore pressure steadily increases as in Fig. 8 and ultimately causes the soil to liquefy. For a hydraulic codictivity of 10^{-3} m/s the excess pore pressure increases only slightly. In that case the permeability is sufficiently high for the drainage to keep up with the compaction, and the pore fluid migrates before it can cause a increase in pore pressure that causes liquefaction.

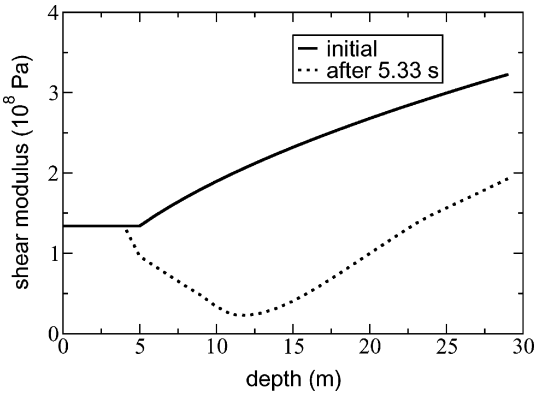

Fig. 9. The shear modulus at $t = 5.33$ s as a function of depth

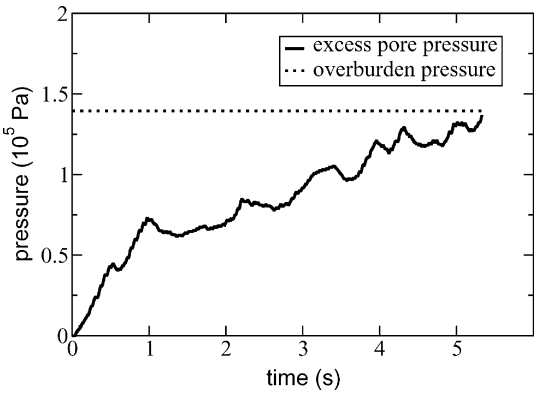

Fig. 10. The excess pore pressure at a depth of 12 m as a function of time

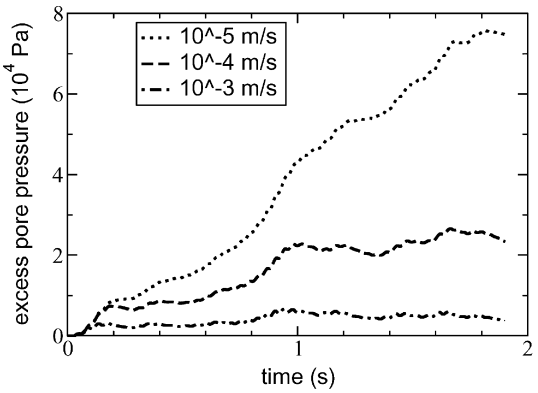

Fig. 11. The pore pressure for three values of the hydraulic conductivity at a depth of 8 m as a function of time

These conclusions can be verified in Fig. 12 in which the shear modulus as a function of depth is shown at $t = 1.9$ s. For a hydraulic conductivity of 10^{-5} m/s the soil liquefies, whereas for $K = 10^{-4}$ and 10^{-3} m/s, respectively, the shear modulus decreases slightly but liquefaction does not occur.

6
Variations in permeability

The numerical simulations of the previous section confirm that the permeability is a key factor in controlling liquefaction. When the permeability has spatial variations it may have an even larger influence on the liquefaction behavior since an impermeable layer can enhance the increase in excess pore pressure. Field observations of this phenomenon have been presented by Youd [38].

In the numerical simulation of Fig. 13 the soil has a hydraulic conductivity of 10^{-3} m/s, except in a layer with a total thickness of 5 m centered at a depth of 10 m. This layer is modelled by the following profile of the hydraulic conductivity:

$$K(z) = K_{max} - (K_{max} - K_{min}) \exp\left(-\frac{(z - z_0)^2}{L^2}\right) , \tag{22}$$

where $K_{max} = 10^{-4}$ m/s, $K_{min} = 2 \times 10^{-6}$ m/s, and $L = 2.8$ m. This describes a low-permeability layer with a

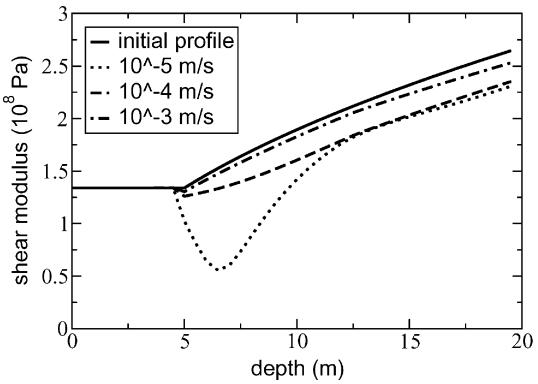

Fig. 12. The shear modulus at $t = 1.9$ s as a function of depth for three values of the hydraulic conductivity

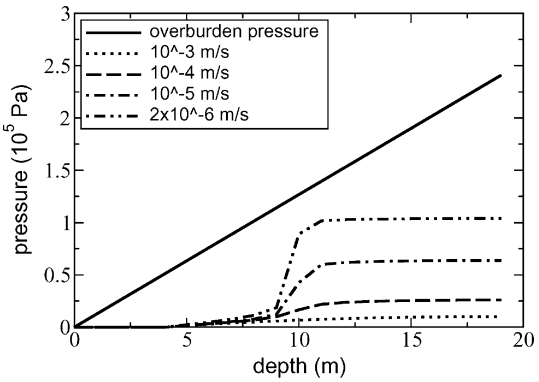

Fig. 13. Excess pore pressure at $t = 5$ s as a function of depth for various values of the hydraulic conductivity K_{min} in the layer. For the hydraulic conductivity of $K_{min} = 10^{-3}$ m/s the layer has the same permeability as the surrounding material (no contrast)

hydraulic conductivity of 2×10^{-6} m/s at a depth $z_0 = 10$ m and an effective width of 5 m. Note that according to the simulation shown in Fig. 12 the soil does not liquefy when the hydraulic condictivity is 10^{-3} m/s throughout the soil.

The excess pore pressure at $t = 5$ s is shown in Fig. 13 for various values of the permeability in the layer. Note that the liquefaction is about to set in when the hydraulic conductivity in the layer is about 10^{-4} m/s or less. The physical reason for this is that the low-permeability layer prevents pore fluid migration towards the surface. Since the pore fluid cannot move out of the bottom of the soil layer, the pore fluid is effectively trapped between the bottom of the model and the low-permeability layer. This causes the excess pore pressure to rise beyond levels that would be found in a homogeneous soil. This confirms that low-permeability layers can have a significant effect on the liquefaction properties of soil [38].

7
Concluding remarks

The liquefaction cycle as introduced in section 2 provides a framework to analyze the complex process of liquefaction into its physical components. This is a reductionists approach [12] that makes it possible to investigate and numerically model the different phenomena that contribute to liquefaction. In this work, the simplest possible physics has been used in the description of the different links of the liquefaction cycle. The advantage of a formulation based on the liquefaction cycle is that one can easily replace the physical description of one of the links in the liquefaction cycle by another description.

The physics of the links in the liquefaction cycle is known with a varying degree of accuracy. The liquefaction cycle can be used as a tool for planning research in the coupled processes that contribute to liquefaction. The dynamic compaction of granular media and the role of pore pressure in this process deserves special attention.

The modelling shown here is applicable only for the onset of liquefaction. Once liquefaction has developed, the fluid migration cannot be described by Darcy's law (5). Also when the liquefaction occurs the shear velocity of

the soil drops and the particle motion increases. In the formulation (13) of Newton's law used here the advective terms $\rho(\mathbf{v} \cdot \nabla \mathbf{v})$ in the equation of motion have been neglected. This is valid only when the particle velocity is much smaller than the wave velocity [39], hence the advective terms in the equation of motion need to be included after the onset of liquefaction. After liquefaction has developed, the rheology (14) should be extended to include plastic flow as well. Dilative arrest may occur once large shears develop.

The onset of liquefaction also creates numerical problems. When the shear modulus goes to zero, the wavelength of the shear waves goes to zero as well. This means that for a fixed spatial discretization, the wavelength becomes smaller than the grid size after the onset of liquefaction, which creates numerical instabilities. There is, however, no reason why the description of the liquefaction cycle used here cannot be used to numerically model the onset of liquefaction in 2 or 3 dimensions.

The numerical experiments presented here show that the scale analysis as applied in section 3 gives the right order of magnitude in its estimation for the range of permeability for which drainage inhibits liquefaction. However, a more detailed modelling is needed to assess the role of drainage in the range of permeability that are relevant for realistic soils. Spatial variations in the permeability have a pronounced effect on the onset of liquefaction when layers with a low permeability inhibits the migration of pore fluid. The numerical modelling technique presented here can be used for the assesment of liquefaction risk [40] as well as for the design of remediation measures [41].

References

1. E. Faccioli, D. Reséndiz, Soil dynamics: behavior including liquefaction. In C. Lomnitz & E. Rosenblueth, editors, Seismic risk and engineering decisions, volume 15 of Developments in Geotechnical Engineering, chapter 4, Elsevier, Amsterdam, (1976), p. 71–139
2. Committee on earthquake engineering. Liquefaction of Soils During Earthquakes. National Academy Press, Washington DC, 1985
3. T.L. Youd, Liquefaction mechanisms and induced ground failure. In W.H.K. Lee, H. Kanamori, P.C. Jennings, & C. Kisslinger, editors, International handbook of earthquake and engineering seismology, part B, Academic Press, (2003), p. 1159–1173
4. G. Castro, Comments on the determination of the undrained steady state strength of sandy soils. In P.V. Lade & J.A. Yamamuro, editors, Physics and Mechanics of Soil Liquefaction, Balkema, Rotterdam, (1999), p. 205
5. J.M. Konrad, A methodology to evaluate the susceptibility of soils for liquefaction flow failures. In P.V. Lade & J.A. Yamamuro, editors, Physics and Mechanics of Soil Liquefaction, Balkema, Rotterdam, (1999), p. 213
6. K. Ishihara, Liquefaction and flow failure during earthquakes. Géotechnique, 43 (1993), p. 351–415
7. B.M. Das, Principles of Soil Dynamics. PWS-Kent Publishing Co., Boston, 1993
8. T.L. Holzer, T.L. Youd, & T.C. Hanks, Dynamics of liquefaction during the 1987 Superstition Hills, California, earthquake. Science, 244 (1989), p. 56–59
9. T. Inazaki, Field measurement of nonlinear propery of the soft ground using a shear wave vibrator. In K. Irikura, K. Kudo, H. Okada, & T. Sasatani, editors, The effects of surface geology on seismic motion, Balkema, Rotterdam, (1998), p. 809–814
10. Z. Yang & A. Elgamal, Influence of permeability on liquefaction-induced shear deformation. J. Eng. Mech., 128 (2002), p. 720–729
11. K. Aki & P.G. Richards, Quantitative Seismology. Univ. Science Books, Sausalito, second edition, 2002
12. D.R. Hofstadter, Gödel, Escher, Bach: an eternal golden braid. Penquin Books, Harmondsworth UK, 1980
13. R.K. Massarch, Deep compaction of granular soils. In W. Shiming, Z. Wohua, and R.D. Woods, editors, A look back for future geotechnics, chapter 5, Balkema, Rotterdam, (2001), p. 181–223
14. M.A. Biot, Consolidation settlement under a rectangular load application. J. Appl. Phys., 12 (1941), p. 426–430
15. J.J. Major, Gravity-driven consolidation of granular slurries; implications for debris-flow deposition and deposit characteristics. J. Sedim. Res., 70 (2000), 64–83
16. H.F. Wang, Theory of linear poroelasticity, with applications to geomechanics and hydrogeology. Princeton Univ. Press, Princeton, 2000
17. H. Nakase, T. Takeda, & M. Oda, A simulation study of liquefaction using dem. In Sêco e Pinto, editor, Earthquake geotechnical engineering. Balkema, Rotterdam, (1999), p. 637–642
18. J.B. Knight, C.G. Fandrich, C.N. Lau, H.M. Jaeger, & S.R. Nagel, Density relaxation in a vibrated granular material. Phys. Rev. E, 51 (1995) p. 3957–3963
19. K. Ishihara, Soil Behaviour in Earthquake Geotechnics, volume 46. Oxford University Press, Oxford, 1996
20. M. Nicolas, P. Duru, & O. Pouliquen, Compaction of granular material under cyclic shear. Eur. Phys. J. E, 3 (2000), 309–314
21. K.L. Gavrilov, Cluster model for compaction of vibrated granular materials. Phys. Rev. E, 58 (1998), p. 2107–2114
22. G. Peng & T. Ohta. Logarithmic density relaxation in compaction of granular materials. Phys. Rev. E., 57 (1998), p. 829–833
23. S.F. Edwards & D.V. Grinev, Statistical mechanics of vibration-induced compaction of powders. Phys. Rev. E, 58 (1998), p. 4758–4762
24. J.J. Brey, A. Prados, & B. Sánchez-Rey, Simple model with facilitated dynamics for granular compaction. Phys. Rev. E, 60 (1999), p. 5685–5692
25. S.J. Linz & Döhle, Minimal relaxation law for compaction of tapped granular matter. Phys. Rev. E, 60 (1999), p. 5737–5741
26. D.A. Head, Phenemenological glass model for vibratory granular compaction. Phys. Rev. E, 62 (2000), p. 2439–2449
27. T.L. Youd, Compaction of sands by repeated shear loading. J. Soil. Mech. and Foundations, 98 (1972) p. 709
28. J.G. Anderson, Strong motion seismology. In W.H.K. Lee, H. Kanamori, P.C. Jennings, & C. Kisslinger, editors, International handbook of earthquake and engineering seismology, part B. Academic Press, (2003), p. 937–965
29. R.O. Davis, & J.B. Berrill, Site-specific prediction of liquefaction. Géotechnique, 48 (1998), p. 289–293
30. J.C. Santamarina, K.A. Klein, & M.A. Fam, Soils and waves. 2001

31. I. Vardoulakis, Deformation of water-saturated sand: II. Effect of pore water flow and shear banding. Géotechnique 46 (1996), p. 457–472
32. K. Terzaghi, The shearing resistance of saturated soils. In Proc. of the First International Conference on Soil Mechanics and Foundation Engineering, volume 1, (1936), p. 54–56
33. H.B. Seed, R.T. Wong, I.M. Idriss, & K. Tokimatsu, Moduli and damping factors for dynamic analyses of cohesionless soils. J. Geotechn. Eng., 112 (1986), p. 1016–1032
34. D.M.F. Chapman & O.A. Godin, Dispersion of interface waves in sediments with power-law shear speed profiles. II. Experimental observations and seismo-acoustic inversions. J. Acoust. Soc. Am., 110, (2001) p. 1908–1916
35. E. Butkov, Mathematical Physics. Addison-Wesley, Reading MA, 1968
36. J. Virieux, SH-wave propagation in heterogeneous media; velocity-stress finite-difference method. Geophysics, 49 (1984), p. 1933–1942
37. G.J. Haltiner & R.T. Williams, Numerical prediction and dynamic meteorology. John Wiley, New York, 1980
38. T.L. Youd, Physics and mechanics of liquefaction from field records and experience. In P.V. Lade & J.A. Yamamuro, editors, Physics and Mechanics of Soil Liquefaction. Balkema, Rotterdam, (1999), p. 325–334
39. R. Snieder, A Guided Tour of Mathematical Methods for the Physical Sciences. Cambridge Univ. Press, Cambridge UK, 2001
40. G.A. Fenton & E.H. Vanmarcke, Spatial variation in liquefaction risk. Géotechnique, 48 (1998) p. 819–831
41. Port and Harbour Research Institute, editors. Handbook on liquefaction remediation of reclaimed land. Balkema, Rotterdam, 1997